15

Mechanisms of Water Transport through Nanoporous Boron Nitride and Graphene Multilayers

Majid Shahbabaei and Daejoong Kim

Department of Mechanical Engineering, Sogang University, 35 Baekbeom-ro, Mapo-gu, Seoul, Republic of Korea, 121-742
*Corresponding author

Outline

Introduction

Demand for potable water is increasing because of the diminishing reliable fresh water sources and the increasing global population. Therefore, it is necessary to explore technologies that can convert nonconventional water sources into fresh water. Seawater is one such abundant source and is accessible by most countries. To utilize seawater as potable water, the high salinity must be eliminated. Desalination technologies are intended for the removal of dissolved salts that cannot be removed by conventional treatment processes. Osmosis is the phenomenon of water flow through a semipermeable membrane that blocks the transport of salts or other solutes. When two aqueous solutions are separated by a semipermeable membrane, water will flow from regions of low solute concentration to regions of high solute concentration. This flow can be stopped or even reversed by applying external pressure to the region of higher concentration. In such a case, the phenomenon is called reverse osmosis (RO). The major advantage of RO is the lower energy consumption due to the absence of an evaporation step. Although the transport process in the solution circulating in the space between the membranes is important, the ion and water transport through the membranes determines the performance of the process. Membranes emerged as a viable means of water purification in the 1960s with the development of high-performance synthetic membranes. Implementation of membranes for water treatment has progressed through the use of more advanced membranes made from new materials and in various configurations. Millions of years ago, nature created biological membranes. The most important feature of a biomembrane is its selective permeability. The size, charge, and other physico-chemical properties of the particles, molecules, atoms, or substances will determine their transport through the membrane. Membranes are thus developed to preferentially permeate species. For this reason, permeation tests are probably the most powerful characterization technique of membranes, and the performance or efficiency of a membrane is dictated by its permeability and selectivity. Recently, novel membranes made of carbon nanotube (CNT) arrays have been investigated for desalination. [1] Although many experimental and theoretical studies have demonstrated that CNTs allow for fast molecule transport rates, [2−7] the low salt rejection rate limits their industrial application. In recent studies, nanoporous graphene, [8−13] graphene oxide, [14,15] and MoS_2 [16] have shown potential as highly selective and permeable filtration membranes. However, to date, only graphene and graphene oxide membranes have been extensively investigated as filtration membranes, and a few groups have attempted the study of BN monolayers. Compared to graphene, BN sheets exhibit high thermal conductivity and stability, electrical insulation, high chemical stability, and high resistance to oxidation. [17−22] Recently, BN nanotubes have shown excellent water permeation potential compared to CNTs of similar length and diameter. [23] Recent experimental studies on graphene oxide have shown that the production of carbon material in molecular-level porous structures with well-tuned pore sizes and interlayer separations could be achieved. [24−27] To date, most studies have investigated water permeation or water desalination through monolayer systems by changing key parameters including nanopore size, chemistry, etc. However, a few studies have investigated water permeation through multilayer nanoporous membranes. [28] Aquaporins (AQPs) have a homotetramer structure with hourglass-shaped subunits. The unique shape of the aquaporin water channels, approximately 20 Å in length and 3 Å in the narrowest diameter at the center of the channel, [29-30] plays a key role in fast water transport. Understanding the flow mechanism in aquaporin water channels can result in achieving high water permeation through semipermeable membranes. Recently, an experimental study using transmission electron microscope (TEM) tomography [31] suggested that solid-state nanopores have more of an hourglass shape than a cylindrical structure. We previously showed that hourglass-

shaped pore structures in multilayer nanoporous graphene (with constant interlayer distances) are a more efficient design for achieving higher flux compared to cylindrical pores. We also found that the hydrophilicity effect can double the flux inside the hourglass-shaped pores. [32] In this chapter, we investigate water transport through hourglass-shaped pores in nanoporous BN and graphene multilayers using MD simulations. In particular, we examine the effect of interlayer spacing on the fast water transport rate.

Simulation Models and Details

We performed MD simulations to investigate the effect of the interlayer distance (d) on water transport through hourglass-shaped pores in multilayer nanoporous boron nitride (BN) and graphene membranes. Graphene and BN structures were generated using the VMD nanotube builder. [33] The models were symmetrically constructed by assembling seven BN and graphene monolayers and replicating the hourglass-shaped aquaporin water channel with diameters ranging from 5 to 8 Å, as shown in Figure 15.1. The graphene and BN layers were introduced by removing adjacent carbon atoms at the center of the layer and selecting pores without sharp edges (see Figure 15.1c for details). The interlayer separation was d = 3.5, 5, 6, and 8 Å. The membranes were connected to a reservoir (31.9 × 34.3 × 30.0 $Å^3$) filled by water molecules. Nonequilibrium MD simulations were performed using the large-scale atomic/molecular massively parallel simulator (LAMMPS) suite. [34] A constant external force f was applied on the water molecules inside the reservoir along the z direction of the layers to model a pressure-driven flow. [35] The simulations were performed in the NVE ensemble (constant number of water molecules, constant volume, and constant energy) with a dissipative particle dynamics (DPD) thermostat36 to maintain a constant temperature of 300 K. A time step of 0.5 fs was chosen to ensure accurate modeling of water molecules between the bulk region and the layers.

Periodic boundary conditions were applied in three dimensions. A cutoff of 10 Å was used for the Lennard-Jones (LJ) potential. The boron and nitride atoms in the BN layers and the carbon atoms in the graphene layers were frozen and considered as uncharged particles to reduce the computational cost. The Lennard-Jones interaction parameters between the water molecules (oxygen) and graphene (C) and boron nitride (B and N) were set as σ_{O-O} = 0.3169 nm and ε_{O-O} = 0.1515 kcal/mol, σ_{O-C} = 0.3190 nm and ε_{O-C} = 0.0956 kcal/mol, σ_{B-O} = 0.3311 nm and ε_{B-O} = 0.12465 kcal/mol, and σ_{N-O} = 0.3267 nm and ε_{N-O} = 0.14965 kcal/mol, respectively. Long-range Coulomb interactions were included using the Ewald method [37] and by applying the SHAKE algorithm, [38] and the water molecules were held rigid. Over 2000 extended simple point charge (SPC/E) water molecules were simulated in the reservoir for 1 ns until an equilibrium state was reached. Next, a pressure difference of 800 MPa was applied across the pores, and nonequilibrium simulations were conducted for 1 ns until a steady-state system was reached. Effective simulation data was subsequently obtained for 5−8 ns nonequilibrium simulations for each layer separation of 3.5, 5, 6, and 8 Å for the graphene and BN systems.

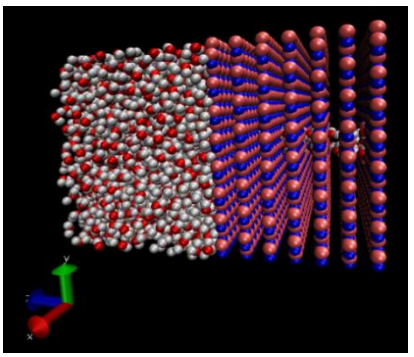

(a)

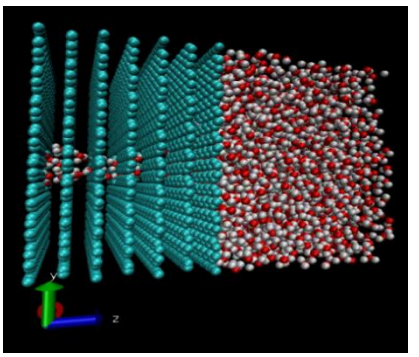

(b)

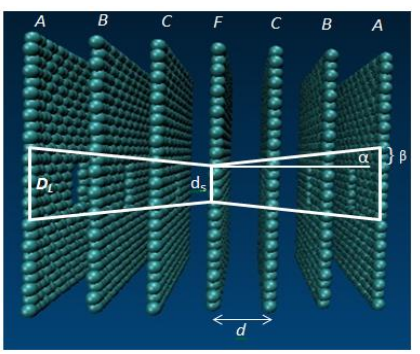

(c)

FIGURE 15.1
Schematic of nanoporous (a) boron nitride (BN) and (b) graphene multilayers with interlayer separation d, (c) graphene multilayers with an hourglass structure. All the nanopore models are symmetrical with the same effective pore diameter. D_L, d_S, d and α are the largest diameter (8 Å), narrowest diameter (5 Å), the interlayer distance, and the cone angle of the hourglass-shaped structure, respectively. Using the relation tanα = β/d, the cone angle α can be determined. Using the cone angle and by changing the interlayer distance, the diameter of the pores located in layers B and C can be estimated

Result and Discussion

Water flux and pair correlation function as a function of layer separation

Water molecules are pushed from the reservoir into the pore system by the applied pressure ΔP, which creates flux and permeability through the membrane. By counting the number of water molecules passing through the multilayers along the z direction, the water flux was calculated. Figure 15.2a shows the variation in water flux as a function of the layer separation for the BN and graphene multilayers. As the layer separation increases, the water flux increases, which is in agreement with recently obtained data. [39] For a layer separation d = 6 Å, the water flux reaches a maximum of 41 and 43 ns^{-1} for the BN and graphene multilayers, respectively. When the layers are widely spaced (d = 8 Å), the water flux decreases in both cases, suggesting that water flux is affected by the energy barrier of the layer separation.

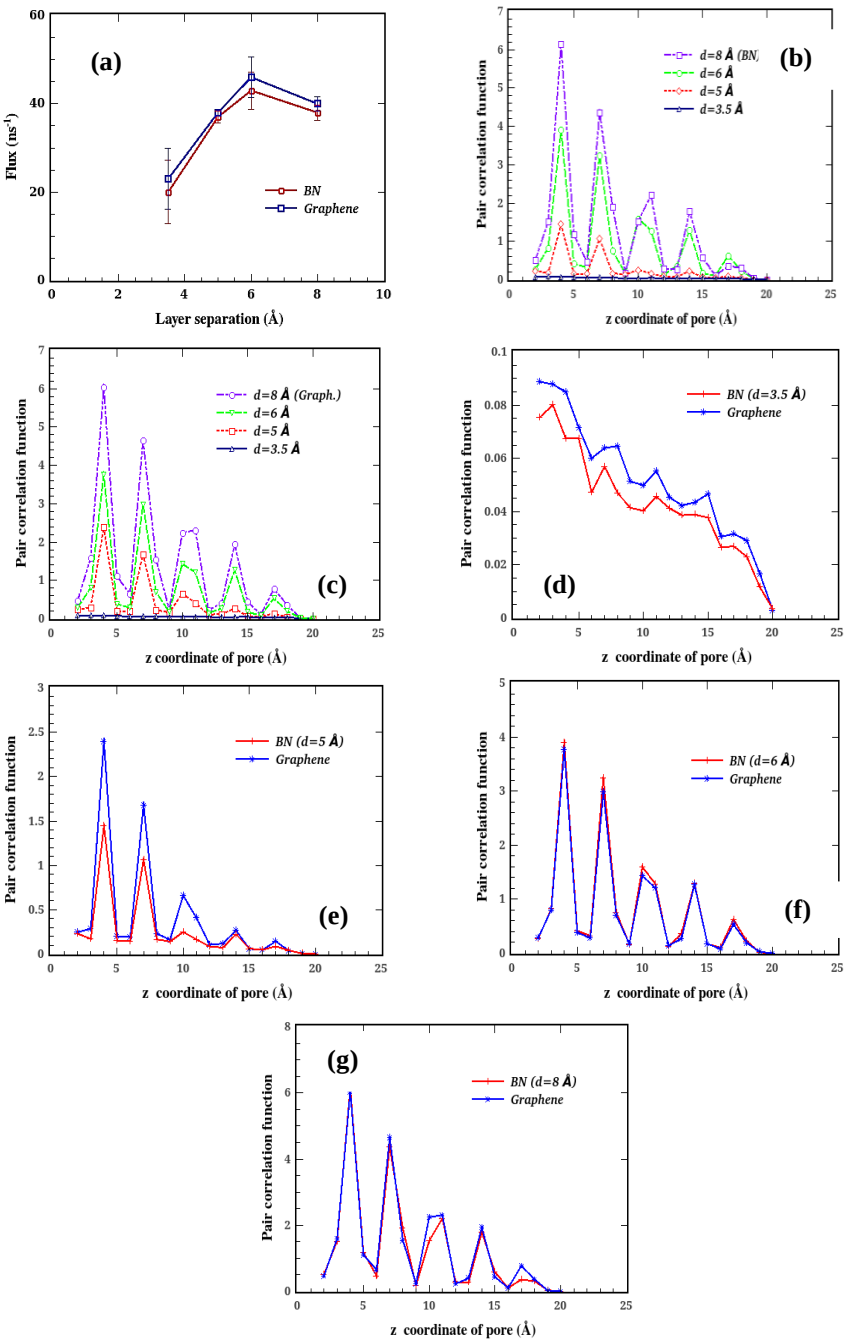

FIGURE 15.2

(a) Water flux as a function of layer separation. Pair correlation function of water molecules inside (b) boron nitride (BN) and (c) graphene as a function of layer separation. Pair correlation function of water molecules inside boron nitride (BN) and graphene with layer separations of (d) d = 3.5, (e) d = 5 Å, (f) d = 6, and (g) d = 8 Å

The water flux through multilayer membranes can thus be maximized by tuning the layer spacing. Moreover, graphene shows higher water flux compared to BN, in agreement with a recent study on water permeation through bilayer BN and graphene. [40] Our results suggest that two factors lead to the smaller flux in BN compared to graphene: the larger friction force and the energy barrier as the gap between layers increases, as explained in the following sections. When the gap between the layers is increased, the water density across the membranes also increases, as evidenced by the pair correlation functions (Figures 15.2b–c). When the layers are strongly stacked (d = 3.5 Å), both BN and graphene have lower densities compared to configurations with larger interlayer distances (d ≥ 3.5 Å) because there is no space for water molecules. When the gap between layers is small (d ≤ 5 Å), BN has a lower density than graphene (Figures 15.2d–e) because of the larger friction force and strong interplay between the water molecules and the wall surface, as discussed in the following section. However, when the layers are sufficiently spaced (d ≥ 6 Å), the density distribution exhibit a similar behavior for both the BN and graphene multilayers (Figures 15.2f–g).

Radial distribution functions (RDFs)

The hydration structure in the BN and graphene multilayers can be illustrated by the radial distribution function (RDF). [41] Figure 15.3a shows the radial distribution functions (RDFs) between the oxygen of water molecules (Ox) and the boron (B) and nitrogen (N) atoms of boron nitride and the carbon atoms of graphene (CG). Although, the RDFs between the water molecules and the surface atoms (a monolayer of BN and graphene) have identical shapes with a minimum located at the same position, the higher intensity of the RDFs for the BN surface suggests more favorable interplay between water and the surface and illustrates the increase in density in the vicinity of the BN surface compared to graphene. Therefore, such a strong interplay between the oxygen of water molecules and the BN surface (high wetting feature of the BN layer) reduces the water transport rate, especially when the layers are strongly stacked (d = 3.5 Å). Figure 15.3b shows the RDFs between the oxygen of water molecules and the BN and graphene multilayers with a layer separation of d = 3.5 Å. The RDF of graphene is zero at short distances, which is due to strong repulsive forces. For both surfaces, the position of the first maximum and the magnitude of the peaks are different, which indicates different hydration numbers. The first peak corresponds to the nearest neighbor shell, and the subsequent maxima suggest the subsequent nearest neighbor shells, which are highlighted for BN. Therefore, strong bridges between the water molecules and BN layers can be formed when the layers are highly stacked (d = 3.5 Å). In addition, to show the layer spacing effect on the hydration structure of the surfaces, the RDFs between the oxygen of water molecules were calculated when the layers were sufficiently spaced.

Figure 15.3c shows the RDFs between the oxygen atoms of the water molecules crossing the BN and graphene surfaces when the layer separation is d = 8 Å. For both surfaces, at short distances, the oxygen−oxygen RDFs have small peaks at the same positions, with high intensity for BN. However, at longer distances, the peaks appear at different positions, and the RDF of graphene is higher than that of BN, suggesting a larger hydration number. We believe that this phenomenon will potentially reduce the energy barriers (the vacant spaces between water molecules) between water molecules inside graphene, which will lead to higher flux than when the layers are widely spaced (d = 8 Å).

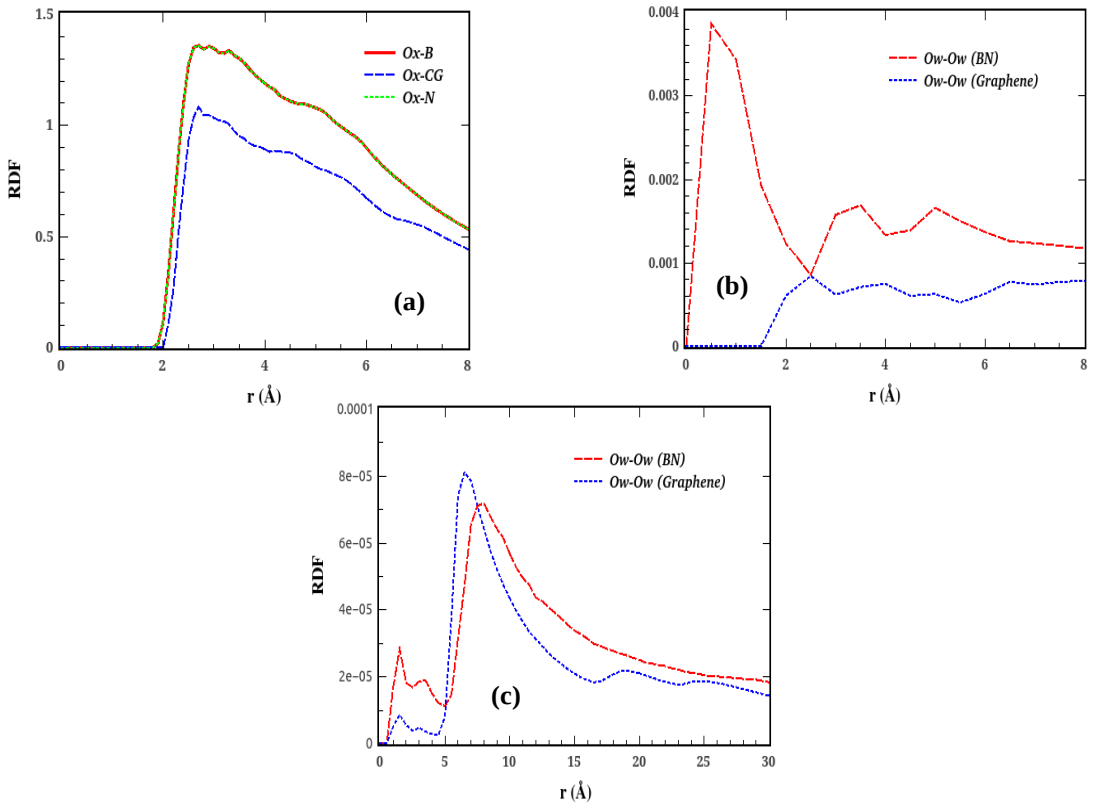

FIGURE 15.3
(a) RDFs between the oxygen of water (Ox) and the boron (B) and nitrogen (N) atoms of boron nitride and the carbon atoms of graphene (CG), and the RDFs between the oxygen of water molecules while crossing the BN and graphene layers with a layer separation of (b) d = 3.5 Å and (c) d = 8 Å

Friction force

The friction force as an interfacial property plays a key role in understanding the transport mechanisms at the nanoscale. Figure 15.4a shows the friction force between water molecules and the BN and graphene surfaces as a function of simulation time when the layers are strongly stacked (d = 3.5 Å). We used a previously described method, [42] where the friction force equals the total tangential force of the pore atoms on the water molecules. Specifically, the friction force at a given time and position is computed as the sum of the forces acting on the wall atoms estimated by the Lennard-Jones potential in the flow direction for the corresponding time step. As shown in Figure 15.4a, the friction force on the two surfaces differs drastically, with the larger friction force occurring on the BN surface. The friction force for BN is larger than that of graphene at the beginning of the simulation and dramatically increases after a short time (~30 ps). This large friction force can reduce the flow rate through BN multilayers for highly stacked layers (d = 3.5 Å). In contrast, the friction force in the graphene multilayers has a lower magnitude and no significant fluctuation during the simulation. The inset shows the difference between the friction forces in BN and graphene for the first 30 ps of the simulation. This larger friction force for BN is in agreement with a recent ab initio study of the friction force of water on graphene and boron nitride sheets. [43] A comparison of the friction force between water molecules and BN surfaces with layer

separations of 3.5 and 8 Å is given in Figure 15.4b. At the beginning of the simulation for d = 3.5 Å, the friction force on graphene is lower, but the friction force on BN drastically increases after a short simulation time (~30 ps). On the other hand, for d = 8 Å, the friction force for BN is larger at the beginning of the simulation but is lower overall compared to the strongly stacked layers (d = 3.5 Å). Therefore, the friction force in the BN multilayer is significantly reduced when the gap between layers is sufficiently increased. Furthermore, the effect of interlayer spacing on the friction force in the BN and graphene multilayers is illustrated in Figure 15.4c. The plot provides a comparison of the friction force between the water molecules and the surfaces as a function of the layer separation. As shown in Figure 15.4c, the friction force decreases as the layer separation increases in the BN multilayer. It also suggests that the friction force in BN will be independent of the layer separation when the layers are sufficiently spaced (d ≥ 5 Å). On the other hand, the plot qualitatively indicates that the friction force in the graphene multilayer will also be independent of the interlayer distance. In addition, for a layer separation of d = 3.5 Å, the BN multilayer has a larger friction force than graphene, which arises from the strong interplay between water molecules and the boron and nitrogen atoms of BN.

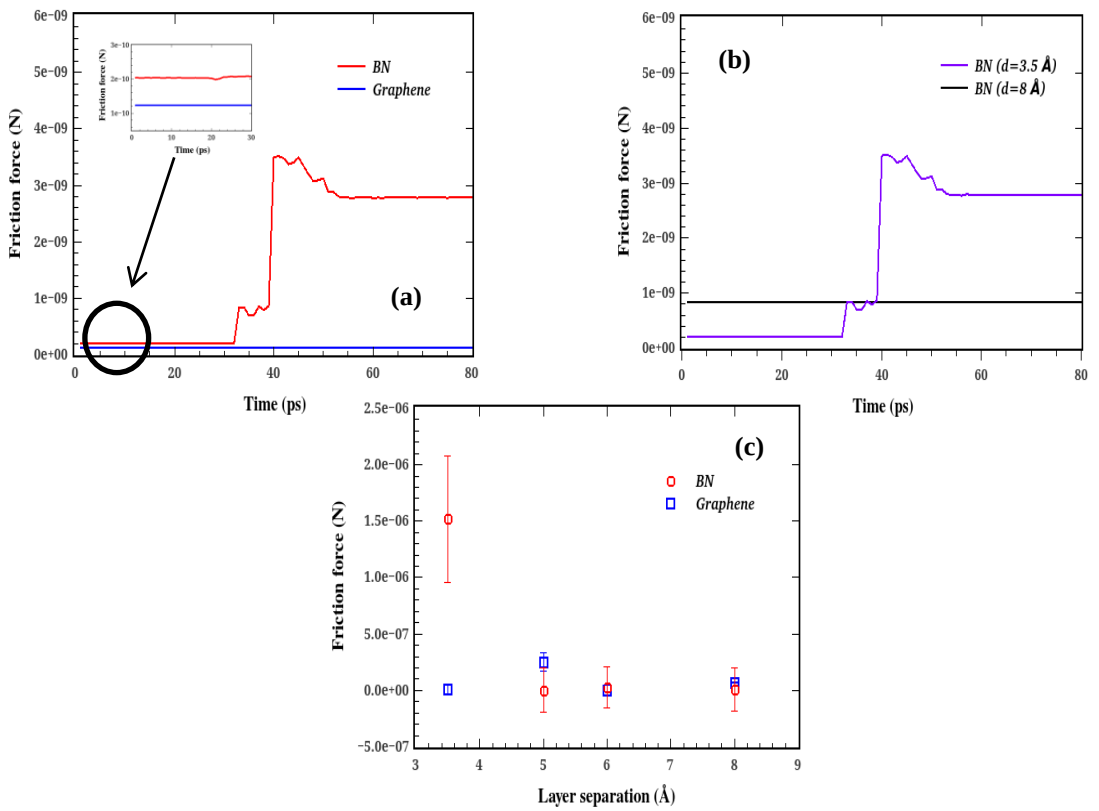

FIGURE 15.4

(a) Friction force between water molecules and the surfaces as a function of time for a layer separation of 3.5 Å, (b) comparison of the friction force between water molecules and the BN surface as a function of time with a layer separation of 3.5 Å and 8 Å, and (c) comparison of the friction force between water molecules and the surfaces as a function of the layer separation

Potential of mean force (PMF)

To monitor the water permeation through the BN and graphene multilayers, one can calculate the potential of mean force (PMF). The radial distribution function (RDF), g(x), describes the variation of the atomic density as a function of the distance from one particular atom. Because density is another way to describe probability, it is also related to the PMF. [44] In fact, we can generate the PMF from the RDF by using the relation PMF(x) = ($-k_BT$)Lng(x). Figure 15.5 illustrates the PMF profiles for water molecules crossing the BN and graphene multilayers with layer separation of 3.5 and 8 Å. As shown in Figure 15.5a, when the layers are strongly stacked (d = 3.5 Å), graphene shows larger PMF compared to BN. However, when the layers are sufficiently spaced (d = 8 Å), BN shows larger energy barriers (more empty spaces between water molecules, which suggest a weak interaction between them) compared to graphene. For d = 3.5 Å, BN exhibits lower energy barriers compared to graphene as well as a smaller water flux, which corresponds to larger friction forces. As shown in Figures 15.4c and 15.5b, rather than the energy barrier, the friction force has a dominant effect on water transport through BN multilayers when the layers are strongly stacked (d = 3.5 Å). When d = 8 Å, BN has a larger energy barrier than graphene. As seen in Figure 15.4c, the friction force in BN is independent of the layer spacing when the layers are sufficiently spaced (d ≥ 5 Å), thus this larger energy barrier (d = 8 Å) might be responsible for the flux reduction in BN compared to graphene.

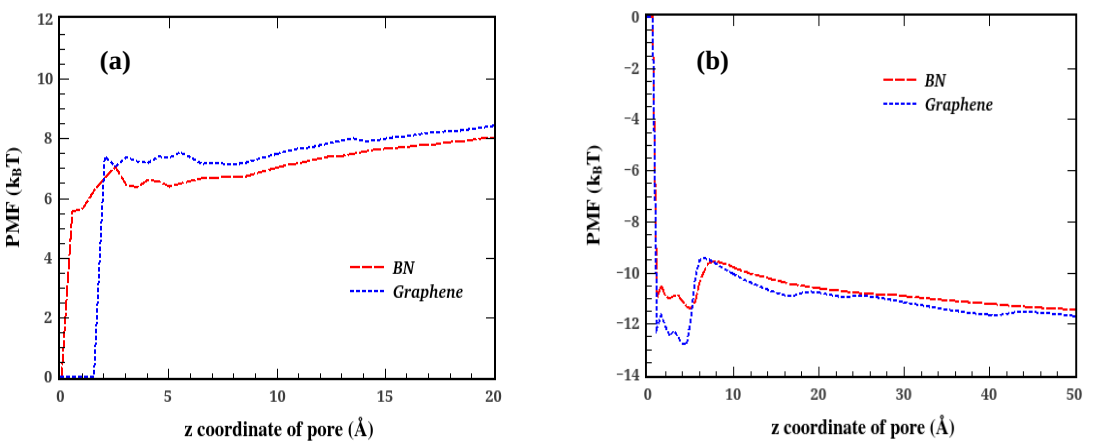

FIGURE 15.5
Potential of mean force (PMF) profiles for water molecules in BN and graphene multilayers with a layer separation of (a) 3.5 Å and (b) 8 Å

Free energy of fluctuation of water molecules and hydrogen bonds

Recently, MD simulations of the free energy of fluctuation, which consists of the thermodynamics of entry of water molecules into CNTs, have been reported. For instance, Pascal et al. [45] reported that the water filling in CNTs is primarily driven by increased rotational and translational entropies for small CNTs and mainly by increased translational entropy for larger CNTs. Sahu et al. [46] have investigated the filling of CNT (6,6) with polar (water) and nonpolar (methane) fluids. They concluded that for both systems, the free energy of transfer from bulk to CNT is favored by increased translational and rotational entropies. They believe that the increase in translational entropy in the confined CNT (6,6) structures is not unique to water-like hydrogen-bonding fluids

but is also observed with nonpolar fluids (such as methane). Kumar et al. [47] explained the effects of temperature and water−carbon interactions on the thermodynamics of filling of narrow CNTs. They observed that both the entropy and energy of transfer decrease with increasing temperature, thereby maintaining the free energy of transfer mostly constant. They also showed that the entropy and energy of the water molecules inside the CNT increase when the attractive part of the LJ interactions between carbon and oxygen atoms is scaled down. Herein, we do not consider the entropy variation on the filling of multilayers; the free energy is obtained using the relation G(N) = −Ln[P(N)]/β, where P(N) is the probability of finding exactly N water molecules inside the pore systems, $\beta = (k_B T)^{-1}$, kB is the Boltzmann constant, and T is the temperature. Figure 15.6a shows the fluctuation of the free energy of occupancy as a function of the number of water molecules inside the BN and graphene multilayers with a layer separation of d = 3.5 Å. The plot shows that the number of water molecules inside BN ranges from 28 to 42 molecules, 36 being the most probable; however, the number of water molecules inside graphene ranges from 35 to 48 molecules, 41 being the most probable.

Compared to BN, the higher occupancy of the graphene multilayer can be attributed to the weak water−water and water−wall interactions, as seen from the RDF data. Figure 15.6b shows the fluctuation of the free energy of occupancy as a function of the number of hydrogen bonds inside the BN and graphene multilayers with a layer separation of d = 3.5 Å. As shown in Figure 15.6b, an increase in the water density between the BN layers can be observed. The wetting characteristics of water on BN surfaces, which arises from the preferential interplay between the water molecules and the surface, will increase the number of hydrogen bonds close to the BN surface, as seen from RDF results. Therefore, high tension between the BN layers arises, as shown by Garnier et al. in their study on bilayer BN.

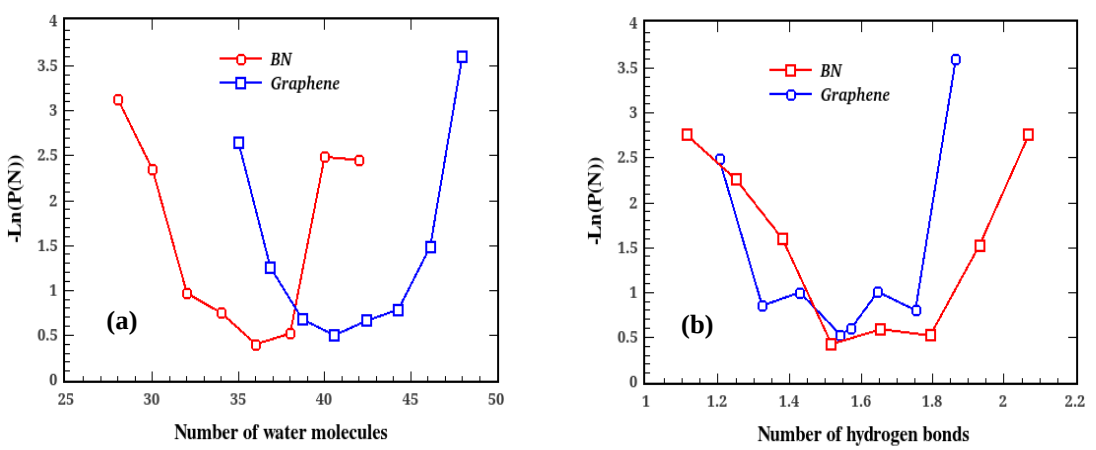

FIGURE 15.6
Fluctuation of the free energy of occupancy as a function of (a) number of water molecules and (b) number of hydrogen bonds in the BN and graphene multilayers with a layer separation of d = 3.5 Å

Diffusion coefficient

Diffusion plays a key role in water transport in confined environments. The axial diffusion coefficient of water molecules can be computed from the mean square displacement (MSD) of the center of mass of the water molecules using $<|(z(t)-z(0))|^2 \geq ADt^n$. [48] In the expression, z denotes

the change in distance along the axial coordinate, A is a dimensional factor (A = 2, 4, and 6 for 1D, 2D, and 3D diffusion, respectively), D is the diffusion coefficient, t is the time interval—which is different from the time step considered in the MD simulations, and n identifies the type of diffusion mechanism. The average diffusion coefficient is computed over all the water molecules inside the system. The time interval is selected to be longer than that of the simulation time step. The largest time interval is equal to the total simulation time, and the smallest time interval is selected to be longer than 50 simulation steps. Figure 15.7a shows the axial diffusion coefficient (A = 2) of the water molecules and the spatial variation of n along the z coordinate of the BN and graphene multilayers when d= 3.5 Å. A similar mechanism indicative of ballistic diffusion can be found for both BN and graphene.

Compared to BN, the water molecules in the graphene multilayer have a higher diffusion coefficient, particularly at the entrance and exit regions. This is due to the weak interplay between water molecules as well as between water and the graphene layers, as seen from the RDF results. Moreover, the larger diffusion coefficient of graphene at the exit region suggests a fast water transport rate, which is consistent with the result presented for the flux. Figure 15.7b shows the axial diffusion coefficient of water molecules along the z coordinate of the graphene multilayer as a function of the layer separation. The axial diffusion coefficient increases as the gap between the layers increases, reaching a maximum of 6.8×10^{-5} cm^2/s for a layer separation of d = 6 Å, which is consistent with the result reported for the flux. Qualitatively, as the interlayer spacing increases, more bulk-like water transport with ballistic diffusion occurs inside the multilayers (see Figures 15.2b–c).

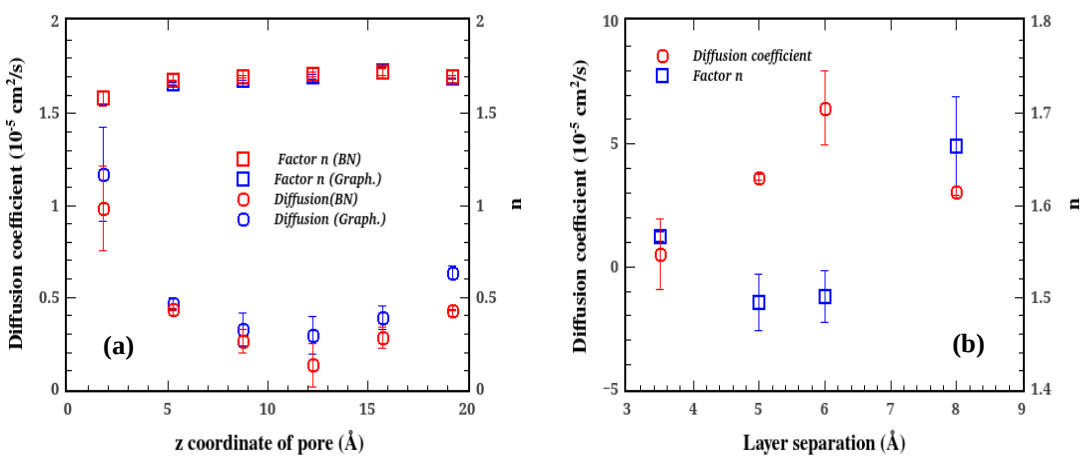

FIGURE 15.7
(a) Axial diffusion coefficient of water molecules and spatial variation of n in graphene and BN multilayers with a layer separation of 3.5 Å, and (b) axial diffusion coefficient of water molecules and spatial variation of n in graphene multilayers with a layer separation of 3.5 Å

Conclusion

We have investigated water permeation through hourglass-shaped pore structures in multilayer nanoporous boron nitride (BN) and graphene using molecular dynamics simulations. In particular, we examined the effect of the interlayer spacing on the water transport mechanism through the

multilayers. We showed that the water flux increases as the interlayer spacing increases, suggesting a maximum of 41 and 43 ns^{-1} in BN and graphene multilayers, respectively, at a layer separation of d = 6 Å. Moreover, the BN multilayer shows less water flux than graphene owing to large friction forces and high energy barriers. Our results show that the friction force on the BN multilayer drastically increases when the layers are strongly stacked (d = 3.5 Å) but is independent of the layer spacing when the layers are sufficiently spaced (d ≥ 5 Å). It is also indicated that the friction force on the graphene surface should be independent of the gap between the layers. On the other hand, when the layers are highly spaced (d = 8 Å), the water molecules in BN have larger energy barriers compared to graphene. Therefore, these two results together indicate that the friction force and energy barriers are both responsible for the flux reduction inside BN in comparison to graphene as the gap between the layers increases. Our results also suggest that the axial diffusion coefficient of the water molecules increases with layer spacing, reaching a maximum of 6.8×10^{-5} cm^2/s at a layer separation of d = 6 Å, which is consistent with the result reported for the water flux. In summary, water permeation through multilayer membranes can be enhanced by properly tuning the distance between the layers.

References

1. Fornasiero, F.; Park, H. G.; Holt, J. K.; Stadermann, M.; Grigoropoulos, C. P.; Noy, A.; Bakajin, O. Ion Exclusion by Sub-2-nm Carbon Nanotube Pores. Proc. Natl. Acad. Sci. U. S. A. 2008, 105, 17250−17255.
2. Holt, J. K.; Park, H. G.; Wang, Y.; Stadermann, M.; Artyukhin, A. B.; Grigoropoulos, C. P.; Noy, A.; Bakajin, O. Fast Mass Transport through Sub-2-Nanometer Carbon Nanotubes. Science 2006, 312, 1034−1037.
3. Majumder, M.; Chopra, N.; Andrews, R.; Hinds, B. J. Nanoscale Hydrodynamics Enhanced Flow in Carbon Nanotubes. Nature 2005, 438, 44.
4. Hummer, G.; Rasaiah, J. C.; Noworyta, J. P. Water Conduction through the Hydrophobic Channel of a Carbon Nanotube. Nature 2001, 414, 188−190.
5. Kalra, A.; Garde, S.; Hummer, G. Osmotic Water Transport through Carbon Nanotube Membranes. Proc. Natl. Acad. Sci. U. S. A. 2003, 100, 10175−10180.
6. Falk, K.; Sedlmeier, F.; Joly, L.; Netz, R. R.; Bocquet, L. Molecular Origin of Fast Water Transport in Carbon Nanotube Membranes: Superlubricity versus Curvature Dependent Friction. Nano Lett. 2010, 10, 4067−4073.
7. Corry, B. Designing Carbon Nanotube Membranes for Efficient Water Desalination. J. Phys. Chem. B 2008, 112, 1427−1434.
8. Nair, R. R.; Wu, H. A.; Jayaram, P. N.; Grigorieva, I. V.; Geim, A. K. Unimpeded Permeation of Water through Helium-Leak-Tight Graphene-based Membranes. Science 2012, 335, 442−444.
9. Cohen-Tanugi, D.; Grossman, J. C. Water Desalination across Nanoporous Graphene. Nano Lett. 2012, 12, 3602−3608.
10. Konatham, D.; Yu, J.; Ho, T. A.; Striolo, A. Simulation insights for Graphene based Water Desalination Membranes. Langmuir 2013, 29, 11884−11897.
11. Sun, C.; Boutilier, MS. H.; Au, H.; Poesio, P.; Bai, B.; Karnik, R.; Hadjiconstantinou, N. G. Mechanisms of Molecular Permeation through Nanoporous Graphene Membranes. Langmuir 2014, 30, 675−682.

12. Wang, E. N.; Karnik, R. Water Desalination Graphene Cleans up Water. Nat. Nanotechnol. 2012, 7, 552−554.
13. Koenig, S. P.; Wang, L.; Pellegrino, J.; Bunch, J. S. Selective Molecular Sieving through Porous Graphene. Nat. Nanotechnol. 2012, 7, 728−732.
14. Kim, H. W.; Yoon, H. W.; Yoon, S.-M.; Yoo, B. M.; Ahn, B. K.; Cho, Y. H.; Shin, H. J.; Yang, H.; Paik, U.; Kwon, S.; et al. Selective Gas Transport through Few-layered Graphene and Graphene Oxide Membranes. Science 2013, 342, 91−95.
15. Li, H.; Song, Z.; Zhang, X.; Huang, Y.; Li, S.; Mao, Y.; Ploehn, H. J.; Bao, Y.; Yu, M. Ultrathin, Molecular-Sieving Graphene Oxide Membranes for Selective Hydrogen Separation. Science 2013, 342, 95−98.
16. Heiranian, M.; Farimani, A.; Aluru, N. Water Desalination with a Single-layer MoS_2 Nanopore. Nat. Commun. 2015, 6, 8616−8622. (17) Golberg, D.; Bando, Y.; Huang, Y.; Terao, T.; Mitome, M.; Tang, C.; Zhi, C. Boron Nitride Nanotubes and Nanosheets. ACS Nano 2010, 4, 2979−2993.
17. Mortazavi, B.; Rémond, Y. Investigation of Tensile Response and Thermal Conductivity of Boron-Nitride Nanosheets using Molecular Dynamics Simulations. Phys. E 2012, 44, 1846−1852.
18. Lei, W.; Zhang, H.; Wu, Y.; Zhang, B.; Liu, D.; Qin, S.; Liu, Z.; Liu, L.; Ma, Y.; Chen, Y. Oxygen-doped Boron Nitride Nanosheets with Excellent Performance in Hydrogen Storage. Nano Energy 2014, 6, 219−224.
19. Sun, Q.; Li, Z.; Searles, D. J.; Chen, Y.; Lu, G.; Du, A. Charge controlled Switchable CO2 Capture on Boron Nitride Nanomaterials. J. Am. Chem. Soc. 2013, 135, 8246−8253.
20. Pakdel, A.; Zhi, C.; Bando, Y.; Golberg, D. Low-dimensional Boron Nitride Nanomaterials. Mater. Today 2012, 15, 256−265.
21. Wang, Y.; Shi, Z.; Yin, J. Boron Nitride Nanosheets: Large-scale Exfoliation in Methane Sulfonic Acid and their Composites with Polybenzimidazole. J. Mater. Chem. 2011, 21, 11371−11377.
22. Won, C.; Aluru, N. Water Permeation through a Subnanometer Boron Nitride Nanotube. J. Am. Chem. Soc. 2007, 129, 2748−2749.
23. Dikin, D. A.; Stankovich, S.; Zimney, E. J.; Piner, R. D.; Dommett, G. H. B.; Evmenenko, G.; Nguyen, S. T.; Ruoff, R. S. Preparation and Characterization of Graphene Oxide Paper. Nature 2007, 448, 457−460.
24. Novoselov, K. S.; Falko, V. I.; Colombo, L.; Gellert, P. R.; Schwab, M. G.; Kim, K. A Roadmap for Graphene. Nature 2012, 490, 192−200.
25. Joshi, R. K.; Alwarappan, S.; Yoshimura, M.; Sahajwalla, V.; Nishina, Y. Graphene Oxide: The New Membrane Material. Appl. Mater. Today 2015, 1, 1−12.
26. Yoon, H. W.; Cho, Y. H.; Park, H. B. Graphene-based Membranes: Status and Prospects. Philos. Trans. R. Soc., A 2016, 374, 20150024.
27. Cohen-Tanugi, D.; Lin, L.-C.; Grossman, J. Multilayer Nanoporous Graphene Membranes for Water Desalination. Nano Lett. 2016, 16, 1027−1033.
28. Agre, P. Aquaporin Water Channels (Noble lecture). Angew. Chem., Int. Ed. 2004, 43, 4278−4290.
29. Jung, J. S.; Preston, G. M.; Smith, B. L.; Guggino, W. B.; Agre, P. Molecular Structure of the Water Channel through Aquaporin CHIP. The Hourglass Model. J. Biol. Chem. 1994, 269, 14648–14654.

30. Kim, M. J.; McNally, B.; Murata, K.; Meller, A. Characteristics of Solid-state Nanometer Pores Fabricated using a Transmission Electron Microscope. Nanotechnology 2007, 18, 205302.
31. Shahbabaei, M.; Tang, D.; Kim, D. Simulation insight into Water Transport Mechanisms through Multilayer Graphene-based Membrane. Comput. Mater. Sci. 2017, 128, 87−97.
32. Humphrey, W.; Dalke, A.; Schulten, K. VDM: Visual Molecular Dynamics. J. Mol. Graphics 1996, 14, 33−38.
33. Plimpton, S. Fast Parallel Algorithms for Short-Range Molecular Dynamics. J. Comput. Phys. 1995, 117, 1−19.
34. Zhu, F. Q.; Tajkhorshid, E.; Schulten, K. Theory and Simulation of Water Permeation in Aquaporin-1. Biophys. J. 2004, 86, 50−57.
35. Groot, R. D.; Warren, P. B. Dissipative Particle Dynamics: Bridging the Gap between Atomistic and Mesoscopic Simulation. J. Chem. Phys. 1997, 107, 4423−4435.
36. Haile, J. M. Molecular Dynamics Simulation: Elementary Methods; John Wiley & Sons Inc: New York, 1997.
37. Ryckaert, J. P.; Ciccotti, G.; Berendsen, H. J. C. Numerical Integration of the Cartesian Equations of Motion of a System with Constraints: Molecular Dynamics of n-alkanes. J. Comput. Phys. 1977, 23, 327−341.
38. Yoshida, H.; Bocquet, L. Labyrinthine Water Flow across Multilayer Graphene-based Membranes: Molecular Dynamics versus Continuum Predictions. J. Chem. Phys. 2016, 144, 234701.
39. Garnier, L.; Szymczyk, A.; Malfreyt, P.; Ghoufi, A. Physics behind Water Transport through Nanoporous Boron Nitride and Graphene. J. Phys. Chem. Lett. 2016, 7, 3371−3376.
40. Frenkel, D.; Smit, B. Understanding Molecular Simulation: from Algorithms to Applications; Academic: San Diego, 2001.
41. Falk, K.; Sedlmeier, F.; Joly, L.; Netz, R. R.; Bocquet, L. Ultralow Liquid/Solid Friction in Carbon Nanotubes: Comprehensive Theory for Alcohols, Alkanes, OMCTS, and Water. Langmuir 2012, 28, 14261–14272.
42. Tocci, G.; Joly, L.; Michaelides, A. Friction of Water on Graphene and Hexagonal Boron Nitride from Ab Initio Methods: Very Different Slippage Despite Very Similar Interface Structures. Nano Lett. 2014, 14, 6872−6877.
43. Yoshida, H.; Mizuno, H.; Kinjo, T.; Washizu, H.; Barrat, J.-L. Molecular Dynamics Simulation of Electrokinetic Flow of an Aqueous Electrolyte Solution in Nanochannels. J. Chem. Phys. 2014, 140, 214701.
44. Pascal, T. A.; Goddard, W. A.; Jung, Y. Entropy and the Driving Force for the Filling of Carbon Nanotubes with Water. Proc. Natl. Acad. Sci. U. S. A. 2011, 108, 11794−11798.
45. Kumar, H.; Dasgupta, C.; Maiti, P. K. Driving Force of Water Entry into Hydrophobic Channels of Carbon Nanotubes: Entropy or Energy? Mol. Simul. 2015, 41, 504−511.
46. Sahu, P.; Ali, Sk. M.; Shenoy, K. T. Thermodynamics of Fluid Conduction through Hydrophobic Channel of Carbon Nanotubes: The Exciting Force for Filling of Nanotubes with Polar and Nonpolar Fluids. J. Chem. Phys. 2015, 142, 074501.
47. Barati Farimani, A.; Aluru, N. R. Spatial Diffusion of Water in Carbon Nanotubes: From Fickian to Ballistic Motion. J. Phys. Chem. B 2011, 115, 12145−12149.